Wind power plant integration in voltage source converter HVdc grids with voltage droop control

S. Añó-Villalba[a,*], R. Blasco-Gimenez[a], S. Bernal-Perez[a], E. Belenguer[b]

[a] *Universitat Politècnica de València, Camino de Vera, s/n; 46022 Valencia, Spain*
[b] *Universitat Jaume I, Av. de Vicent Sos Baynat, s/n; 12071 Castelló de la Plana, Spain*

Abstract

This paper introduces the use of a diode-based HVdc rectifier for the integration of a large off-shore wind power plant into an existing HVdc voltage source converter-based grid by means of an uncontrolled rectifier. Optimal HVdc voltage droop gains have been proposed to minimize the power line losses. The proposed control system allows for the wind power plant to energize the complete HVdc grid, in order to contribute to service restoration in the case of a black-out. The system exhibits good response to wind power plant black-start operation, rectifier breaker trip and reclosure, and short-circuit ride through at the on-shore ac-grid. The technical feasibility of the proposed topology has been validated by means of detailed PSCAD simulations using frequency dependent parameters for cable modeling.

Keywords: Wind power generation, HVdc grid, Voltage source converter, Voltage droop control.

1. Introduction

One of the European energy goals is to maximise wind energy in electricity mix [15] and to reinforce the grid infrastructure, specially through off-shore HVdc grids according to European Horizon 2020 LCE-5 action. In this sense, the integration of large wind power plants (WPP) in HVdc grids has been the subject of active research during recent years. Different alternatives have been object of study, including the use of HVdc Voltage Source Converters (VSC) [20, 19, 25], HVdc Current Source Converters (CSC) [14, 10, 29] or a combination of the two [26]. Recently the world's first multiterminal VSC HVdc system (±160 kV) has been put into operation for WPP integration to HVdc grids [31].

Diode-based rectifiers for unidirectional HVdc links have been suggested in the past as an alternative to increase efficiency and system reliability [21, 16]. Specifically, diode rectifiers have been proposed for the connection of single unit generators to HVdc grids with Line Commutated Converters (LCC) in order to achieve reduced losses, decreased complexity and enhanced reliability [7].

Previous author's work has shown that a diode-based HVdc rectifier is a feasible solution for the point-to-point connection of large off-shore WPP using inverter stations based on Line Commutated Thyristors (LCT) [5, 6] or on VSCs [4]. These topologies use the wind turbine front-end converters to control the off-shore ac-grid voltage and frequency, as well as the power delivered to the HVdc link. Moreover, the wind turbines converters also contribute to current limitation during faults.

The main innovations of this paper when compared to author's previous work are: 1. HVdc voltage droop control, minimizing cable losses, 2. Cable modeling with distributed parameters, for fast transient simulation, 3. New scenarios, as WPP start-up with with cable and VSC capacitor charging, and cable pole-to-ground fault.

The diode-based HVdc rectifier integration to HVdc grids must overcome some significant challenges: network restoration issues, compliance with grid codes and control strategies to ensure the power flow inside the network [11].

*Corresponding author
Email address: sanyo@die.upv.es (S. Añó-Villalba)
[1] doi: http://dx.doi.org/10.1016/j.matcom.2016.12.007

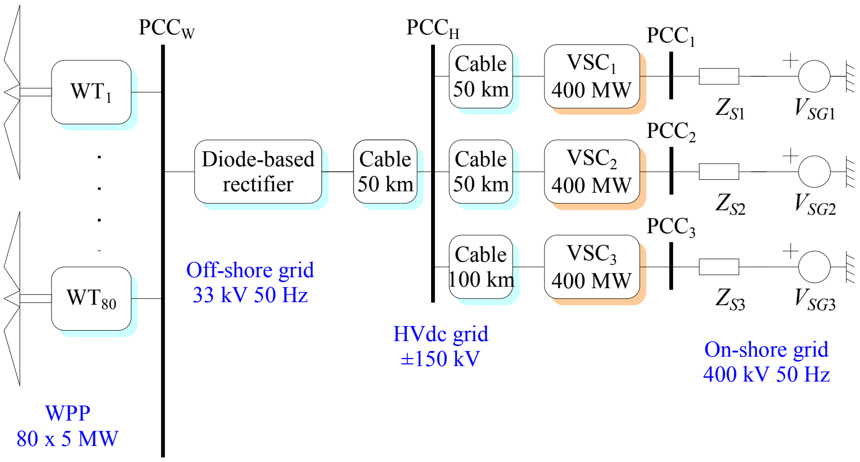

Figure 1: Diode-based rectifier for the connection of the 400 MW off-shore WPP to the HVdc grid and three 400 MW VSCs.

This paper will asses the technical feasibility integration of WPP and VSC stations in HVdc grids. This is accomplished in both quasi-steady state (energization) and transient (faults) modes. The proposed system has four bipolar terminals connected to a radial HVdc grid with metallic return: three VSCs and one WPP connected through diode rectifiers. During normal operation, two of the VSCs control the direct voltage of the HVdc grid by means of voltage droop control. The droop constants are chosen to minimize the HVdc grid losses and, although this technique has been already proposed in [27, 2], the control does not need communication between stations.

The most challenging system faults are those in the HVdc-grid due to the free-wheeling diodes of the VSCs. Research has been made about short-circuit faults in the HVdc link [12], including fault location [30] and protection [9, 13]. The contributions of this paper are the analysis of the pole-to-ground fault taking into account the grounding of the bipolar system, and the system operation at reduced power after the fault.

The proposed control strategies are validated by means of detailed PSCAD/EMTDC simulation of different scenarios: HVdc link energization, WPP rectifier trip and reclosure, pole-to-ground fault, and three-phase on-shore short-circuit with grid support.

2. System description

2.1. Wind power plant and HVdc terminals

The proposed system consists of a HVdc grid with four terminals, fig. 1. One of the terminals is a diode-based rectifier connected to an off-shore WPP with eighty 5 MW-rated wind turbines. The WPP is modeled using five ($i = 1, 2, ..5$) wind turbine clusters, fig. 2, of 5, 40, 80, 120 and 155 MW. Each wind turbine has a permanent magnet synchronous machine direct drive generator. The generator is connected to the Point of Common Coupling PPC$_\mathrm{W}$ through the full scale back-to-back converter and the wind turbine transformer $\mathrm{T_{Wi}}$. The table in the Appendix shows the system parameters. The uncontrolled rectifier shown in fig. 3 connects the WPP to the HVdc grid at PCC$_\mathrm{H}$ using submarine cables. Z_{FR} represents the capacitor and filter banks of the rectifier and $\mathrm{T_{R1}}$ and $\mathrm{T_{R2}}$ are the rectifier transformers. The rectifier is a bipolar 12-pulse diode-based type. L_R is the rectifier smoothing reactor. The breaker $\mathrm{BK_R}$ disconnects the WPP from the rectifier transformer and the breaker $\mathrm{BK_{R1}}$ disconnects only the positive pole.

The subscripts p and m stand for positive and negative poles respectively and are removed in normal operation as the system is balanced, e.g. $E_R = E_{R,p} + E_{R,m}$ will be the voltage between poles.

The other three terminals of the HVdc system consist of three ($j = 1, 2, 3$) identical bipolar VSCs connected to the on-shore ac-grid at PCC$_\mathrm{j}$, fig. 4. Each terminal has two step-up transformers $\mathrm{T_{Vj}}$. The on-shore ac-grid is modeled with a simple Thevenin's equivalent (Z_{Sj} and V_{SGj}) but with the challenge of weak ac-grid parameters as

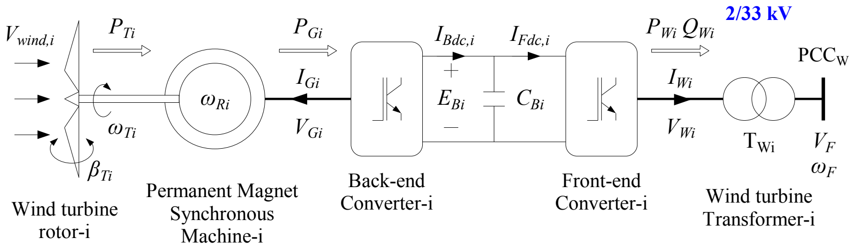

Figure 2: Wind turbine cluster i ($i = 1, 2, ..5$) connected to the off-shore PCC$_W$.

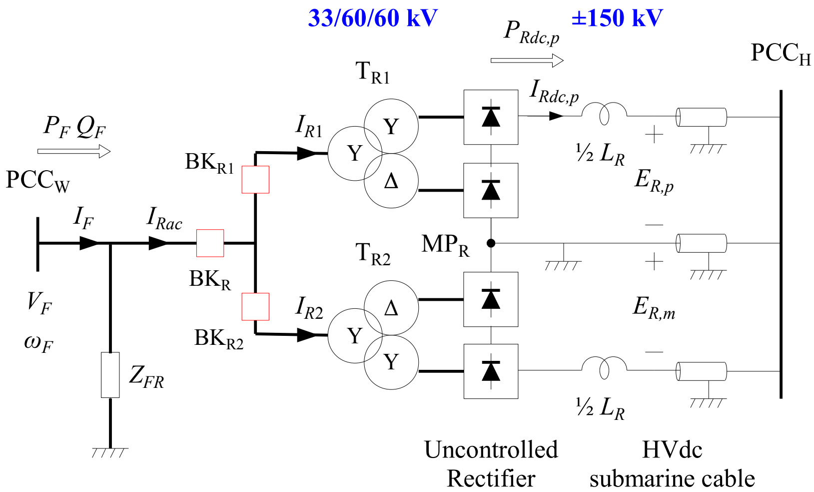

Figure 3: Off-shore uncontrolled rectifier connected to PCC$_H$ through submarine cables.

$S_{cc,j} = 2.0$ pu. According to [18] a weak grid has a SCR less than 3 and in this paper:

$$SCR_j = \frac{S_{Scc,j}}{P_{V,base}} = \frac{2.0 \times 500 \text{ MVA}}{400 \text{ MW}} = 2.5 < 3 \tag{1}$$

The midpoints (MP) of the bipolar terminals are connected to each other through a metallic return. This configuration is similar to that in Crete island [17] where the system can operate at reduced power after a pole to sheath fault. All the midpoints are grounded, that is, connected to earth. The sheaths of the cables are also grounded at both ends.

2.2. *HVdc submarine cable*

Fig. 5 shows the cross-section of the HVdc link submarine cable. The simulation of fast electromagnetic transients requires frequency dependent parameters for cable modeling. Cable parameters are calculated by dedicated cable-constants (CC) support routines using cable geometry and material properties data. The input data needs some preparation due to the differences between the real cable design and that represented by the CC support routines, e.g. the insulation relative permittivity includes the influence of the two semiconductor layers [22] which are around the insulation (not shown in this figure).

Table 1 shows the parameters for a 150 kV 200 MW submarine cable installed at moderate climate [1] and the corresponding MV metallic return. The gaps in manufacturer data were filled with data based in [24] and [8].

All cables are 50 km length except the one that connects VSC$_3$ with PCC$_H$, fig. 1, which is 100 km length.

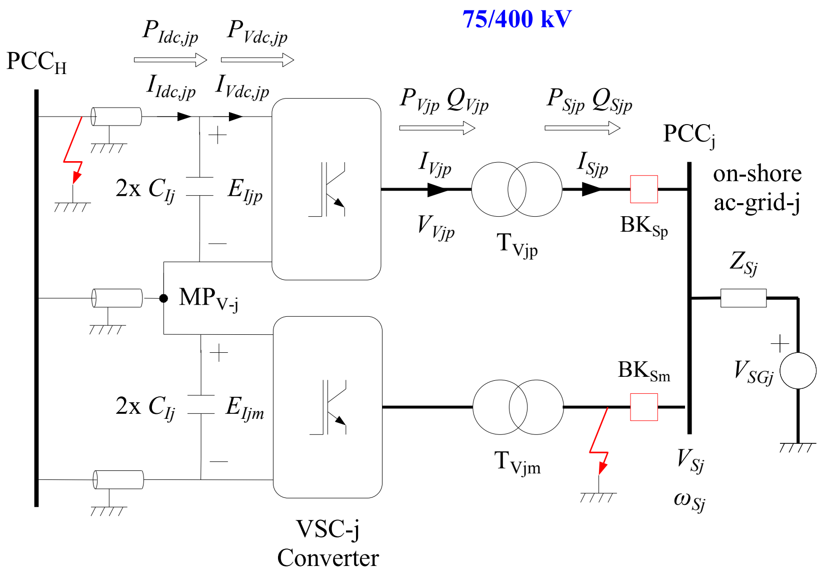

Figure 4: VSC j ($j = 1, 2, 3$) terminal connected to the on-shore PCC$_j$ and ac-grid j.

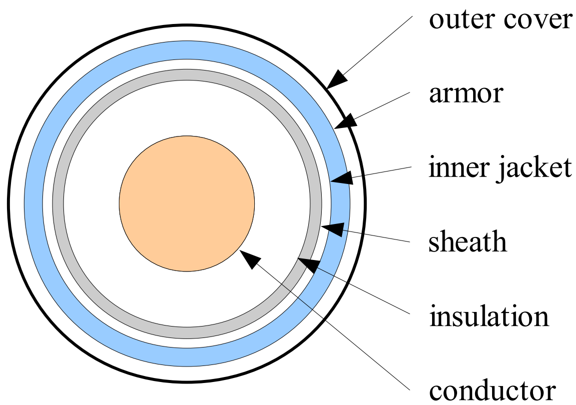

Figure 5: HVdc submarine cable cross section.

Table 1: HVdc XLPE Submarine Cable Parameters

Layer	Material	Radius (mm)		ρ (nΩm)	ϵ_r	μ
		pole	return			
Conductor	Copper	18.2	18.2	17.6		1
Insulation	XLPE	33.2	27.2		2.5	1
Sheath	Lead alloy	36.2	30.2	220		1
Inner jacket	PE	38.8	32.8		2.3	1
Armor	Galvanized steel	43.8	37.8	180		10
Outer cover	PP	48	42		2.2	1

3. Wind power plant and voltage source converter controls

3.1. Wind power plant and voltage source converter power controls

The different system voltages are set as follows during normal operation. The on-shore ac-voltages V_{Sj} are set by the on-shore ac-grids represented by V_{SGj}. The HVdc grid voltages E_{Ij} and E_R are set by VSC1 and VSC3 using

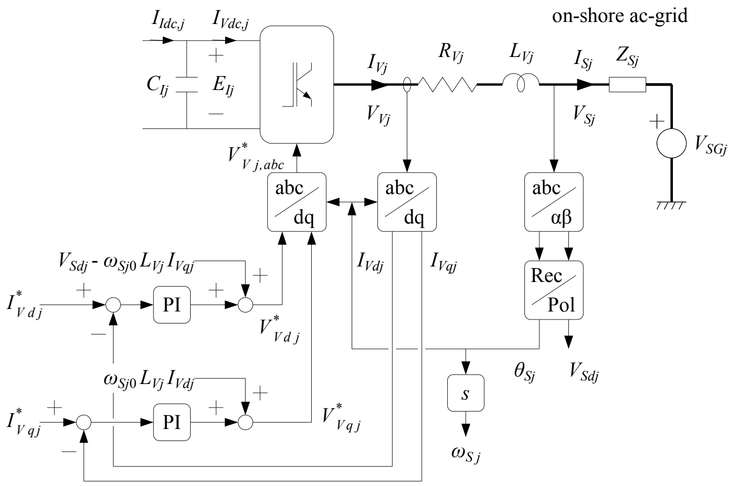

Figure 6: Current control loops of VSC j, $j = 1, 2, 3$.

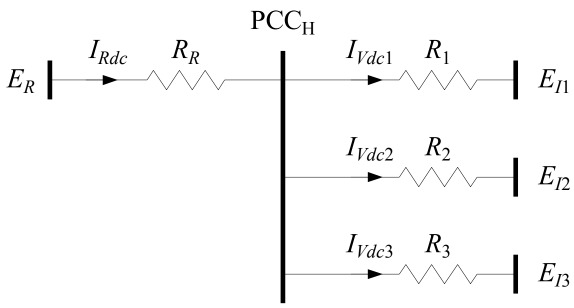

Figure 7: HVdc cables in steady state.

a voltage droop control. Finally, the off-shore ac-voltage V_F is clamped to the HVdc link voltage through the diode rectifier.

The wind turbines limit their front-end active currents $I_{Wd,i}$ in order to operate at optimum power tracking. When these currents are not limited, e.g. during WPP sudden disconnection, they control the off-shore ac-grid voltage V_{Fd}. Moreover, the off-shore ac-grid frequency is controlled by the front-end reactive currents $I_{Wq,i}$. A detailed description of these controls and the proper current sharing between the wind turbines can be found in [6].

The on-shore VSC2 operates generating the active and reactive powers following their references. The reactive power reference changes from normal operation to grid support when a short-circuit occurs at PCC_2. The power controls are achieved by inner current (I_{Vd2} and I_{Vq2}) control loops, fig. 6. A detailed description of the control loops can be found in [3].

3.2. *HVdc grid voltage droop control*

The on-shore terminals VSC1 and VSC3 control the HVdc grid voltages $E_{I1,3}$ using the inner current ($I_{Vd1,3}$) control loops shown in fig. 6 and described in [3]. Therefore they will evacuate the active power injected to the HVdc link by both the WPP and the VSC2. In this paper, the power sharing between VSC1 and VSC3 is made choosing the currents $I_{Vdc1,3}$ in order to minimize the power losses in VSC1 and VSC3 HVdc cables. From fig. 7:

$$I_{Rdc} = I_{Vdc1} + I_{Vdc2} + I_{Vdc3} \tag{2}$$

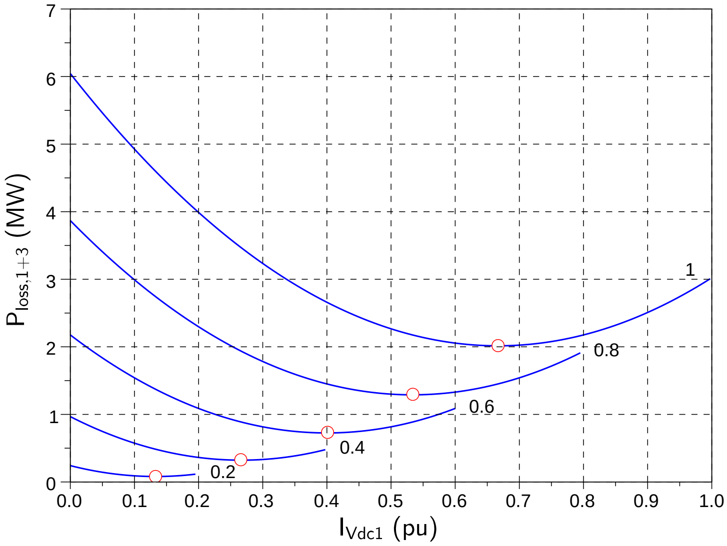

Figure 8: Power losses at HVdc cable as a function of I_{Vdc1} and $(I_{Rdc} - I_{Vdc2}) = 0.2, 0.4, ..1$ (pu).

then the power losses as a function of I_{Vdc1} are:

$$P_{loss,1+3} = R_1 I_{Vdc1}^2 + R_3(I_{Rdc} - I_{Vdc1} - I_{Vdc2})^2 \tag{3}$$

where $R_{1,3}$ are the dc-resistances of submarine cables from the VSC1,3 to $\mathrm{PCC_H}$. The current I_{Vdc1} that minimizes the above expression is:

$$I_{Vdc1,min} = \frac{R_3}{R_1 + R_3}(I_{Rdc} - I_{Vdc2}) \tag{4}$$

From equations (2), (3) and (4), fig. 8 shows graphically that a minimum value exists for different values of $(I_{Rdc} - I_{Vdc2})$.

In a similar way:

$$I_{Vdc3,min} = \frac{R_1}{R_3 + R_1}(I_{Rdc} - I_{Vdc2}) \tag{5}$$

and for each operating point, the minimum power losses are guaranteed if:

$$I_{Vdc1} = \frac{R_3}{R_1} I_{Vdc3} \tag{6}$$

The desired currents are set using voltage droop control:

$$I^*_{Vdc1,3} = k_{droop1,3}\left(E_{I1,3} - E_{Ilow1,3}\right) \tag{7}$$

where the direct voltages are:

$$E_H = R_{1,3} I_{Vdc1,3} + E_{I1,3} \tag{8}$$

From equations (6), (7) and (8), minimum losses requires:

$$\frac{R_3}{R_1} = \frac{k_{droop1}\left(E_H - E_{Ilow1}\right)\left(1 + k_{droop3}R_3\right)}{k_{droop3}\left(E_H - E_{Ilow3}\right)\left(1 + k_{droop1}R_1\right)} \tag{9}$$

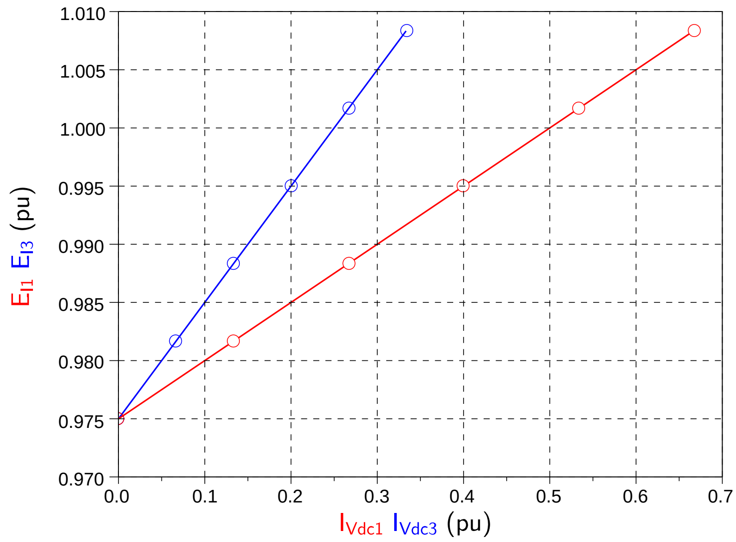

Figure 9: HVdc voltage droop control equations (7).

In this paper no communications are needed between the two terminals to minimize the HVdc cable power losses at each operating point of the HVdc grid. This is achieved by choosing $E_{Ilow1} = E_{Ilow3}$, which yields:

$$k_{droop1} = \frac{R_3}{R_1} k_{droop3} \tag{10}$$

that is, equation (6) is satisfied for every operating point when $k_{droop1,3}$ are selected according to (10).

With $E_{Ilow1} = E_{Ilow3} = 0.975$ pu, direct voltage values will be close to 1 pu because of the voltage droop controls of VSC1,3, fig. 9. Note that $I_{Vdc1} + I_{Vdc3} = I_{Rdc} - I_{Vdc2} = 0$ to 1 pu.

Finally the inner control loop current references $I^*_{Vd1,3}$ can be obtained by power balance in VSC1,3 neglecting losses:

$$E_{I1,3} I^*_{Vdc1,3} = 3(V_{Vd1,3} I^*_{Vd1,3} + V_{Vq1,3} I_{Vq1,3}) \tag{11}$$

4. System performance

The proposed system model and control techniques have been validated using PSCAD simulations. The base power of the HVdc system is 400 MW and the base voltages are 2/33 kV for the wind turbine transformers (T_{Wi}), 33/61 kV for the diode-based rectifier transformers (T_{R1} and T_{R2}), and 75/400 kV for the on-shore VSC transformers (T_{Vj}). The table in the Appendix shows the system parameters.

Submarine cables have been modeled in PSCAD by using the “Frequency Dependent (Phase)” model together with “Cable Constants Coax Cable Data” which uses data from Table 1. This model is based on fitting the matrices for propagation and the characteristic admittance in the phase domain, [23], and is accurate for fast transients, e.g. the scenario of section 4.4.

This section analyzes the system performance under different scenarios. Except when noted, the results are shown in pu and the default reference values are as follows: $\omega^*_F = 50$ Hz, $V^*_{Fd} = 1.1$ pu which, together with I_W current limits, ensures that the WPP operates in current control mode, $Q^*_{S2} = 0$ pu except when grid support is needed, and $P^*_{S2} = 0$ pu to highlight P_{S1} and P_{S3} power sharing due to the voltage droop control.

4.1. System energization and support to service restoration

Smooth system energization can be done using the energy from the WPP because the rectifier terminal can operate in current control mode. The elements to energise are the capacitor and filter banks of the rectifier, the submarine cable

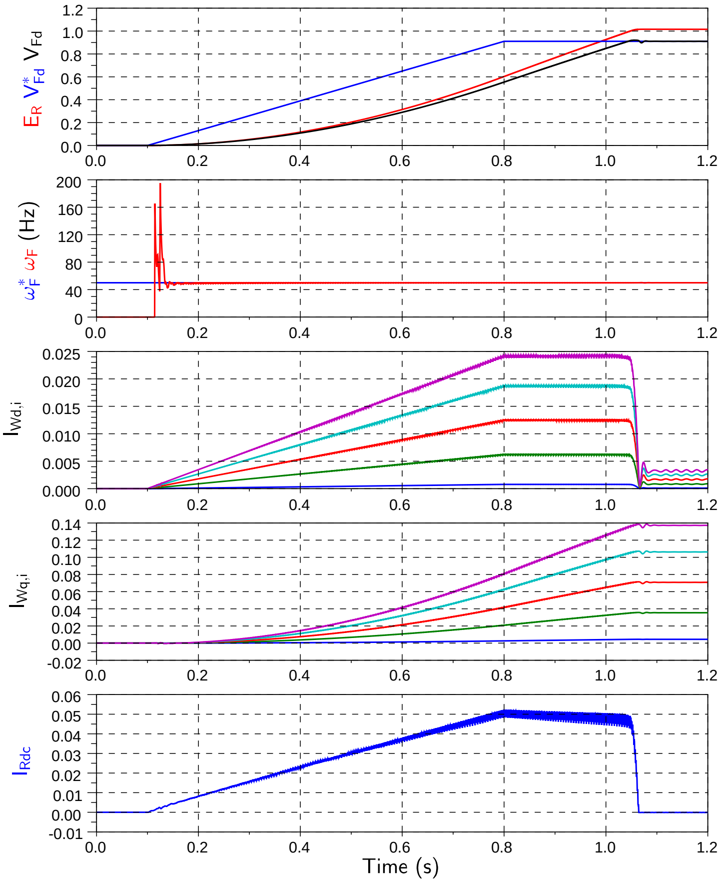

Figure 10: System energization using the WPP.

capacitance and, what's more important, the VSC capacitors without the need of limiter resistors. Fig. 10 shows the system response during energization. The reference V_{Fd}^* ramps up from 0 pu to the value V_{Fd0} that ensures full charging of VSC capacitors, e.g. $E_R = 1$ pu which according to [18] is:

$$V_{Fd0} = \frac{\pi E_R}{3\sqrt{6}BN} = \frac{\pi \times 300}{3\sqrt{6} \times 4 \times 61/33} = 0.9104 \text{ pu} \tag{12}$$

Smooth system response is obtained because from $t = 0$ to $t = 1.05$ s the active currents $I_{wd,i}$ are limited so the rectifier terminal is in current control mode. Therefore the ac-grid voltage V_{Fd} can not follow its reference until $t = 1.05$ s when the I_{Rdc} current decreases to 0 pu as the HVdc link and VSC capacitors are already charged. This figure also shows the good current sharing between the five wind turbine clusters. After system energization the active currents $I_{wd,i}$ keep an small value because of rectifier filter losses, and reactive currents $I_{wq,i}$ must absorb the reactive power from the rectifier capacitor and filter banks.

The ω_F glitches from $t = 0.11$ to 0.14 s are not relevant as the corresponding voltage V_{Fd} is very low, less than 0.003 pu.

4.2. *HVdc rectifier breaker trip and reclosure*

The WPP will be disconnected if the breaker located between the rectifier transformer and the filter banks ($\mathrm{BK_R}$) is suddenly opened. The system response to the breaker trip at rated power and reclosure is shown in fig. 11.

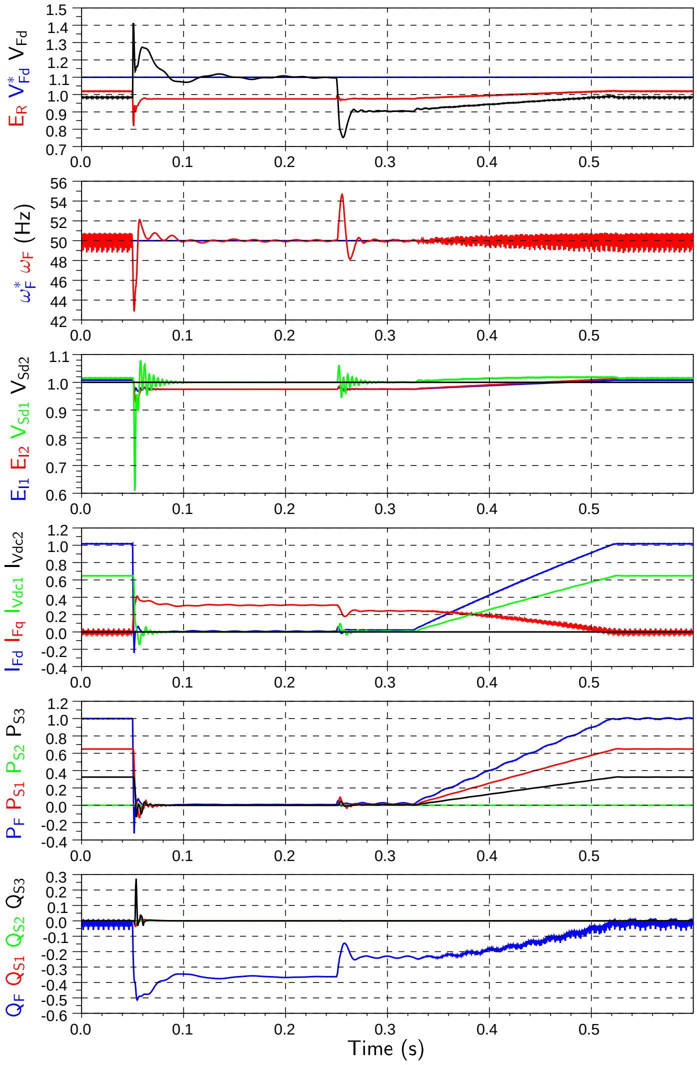

Figure 11: System response to rectifier breaker trip and reclosure.

At t = 50 ms the breaker is opened and the current I_{Fd} is reduced to about 0 pu and so does the WPP production. However the current I_{Fq} increases to about 0.3 pu to absorb the reactive power generated by the rectifier capacitor and filter banks. During the disconnection the WPP control is able to follow both references V^*_{Fd} and ω^*_F.

The voltage V_{Fd} shows a 1.4 pu overvoltage during 2 ms due to the fast change in the front-end currents (I_{Wi}) which is similar to that in I_{Fd}. This overvoltage must be mitigated by surge arresters in the capacitor and filter banks.

The WPP power P_F shows a negative value of 0.32 pu during less than 2 ms when the breaker opens. The equivalent energy of 90 kJ must be dissipated in the back-to-back brake resistors of the wind turbines.

At t = 250 ms the breaker is closed and the WPP production is smoothly increased again to its rate power.

4.3. VSC2 short-circuit with reactive power injection

When a three-phase short-circuit occurs at the on-shore PCC$_2$, the voltage V_{Sd2} is suddenly reduced, fig. 12. As a consequence of it, the VSC2 can not evacuate power and P_{S2} decreases from 0.5 pu to 0 pu. Then all the WPP production is evacuated through VSC1 and VSC3.

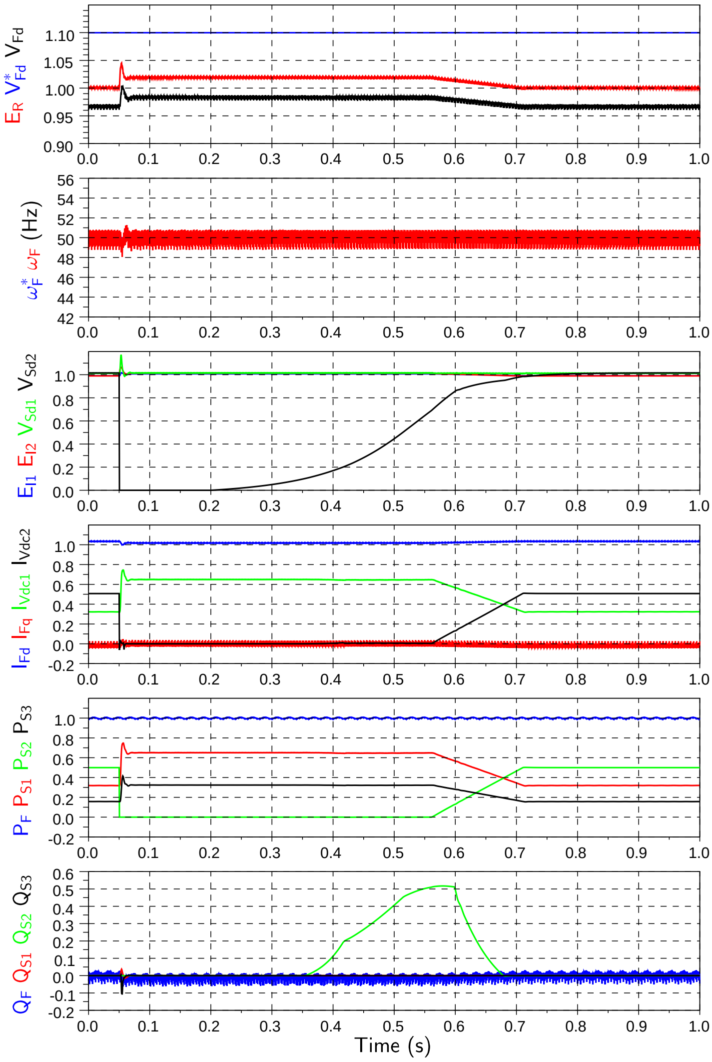

Figure 12: System response during short-circuit at PCC$_2$.

For protection purposes, a Voltage Dependant Current Order Limit (VDCOL) reduces the current limit $|I_{V2}|_{max}$ as a function of the measured value of V_{Sd2}, fig. 13. Moreover, to provide grid support during the short-circuit, the control of the reactive power Q_{S2} is considered as a priority, so the current limit is distributed as follows:

$$I_{Vq2,\text{max}} = |I_{V2}|_{\text{max}} \tag{13}$$

$$I_{Vd2,\text{max}} = \sqrt{|I_{V2}|^2_{\text{max}} - I^2_{Vq2}} \tag{14}$$

The VDCOL mechanism in VSC2 reduces the current $|I_{V2}|$, thereby decreasing I_{Vdc2} to 0 pu and isolating the short-circuit from the HVdc link. Because of this, during the short-circuit the HVdc voltage control droop is able to keep the dc-voltage close to its rated value. Also the off-shore ac-grid voltage and frequency are under control. The result is that the WPP production is not affected by the short-circuit.

When the voltage V_{Sd2} starts rising, VSC2 injects reactive power (Q_{S2}) for grid support purposes. The VSC2 control can be programmed according to the code grid that applies. The VDCOL ensures the smooth VSC2 restoration to the initial state; see the current I_{Vdc2} and the power P_{S2} ramps in fig. 12.

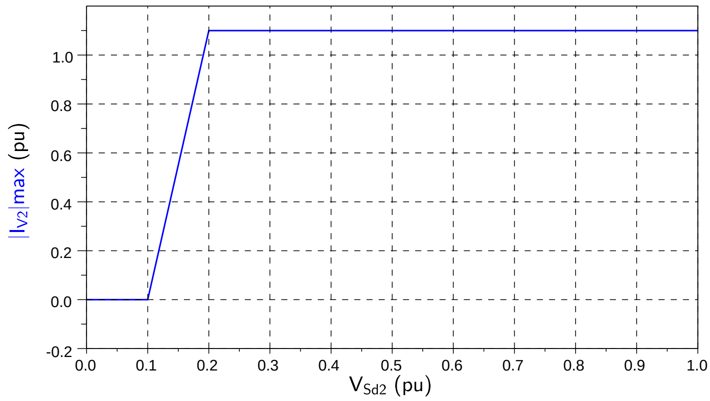

Figure 13: VDCOL characteristics.

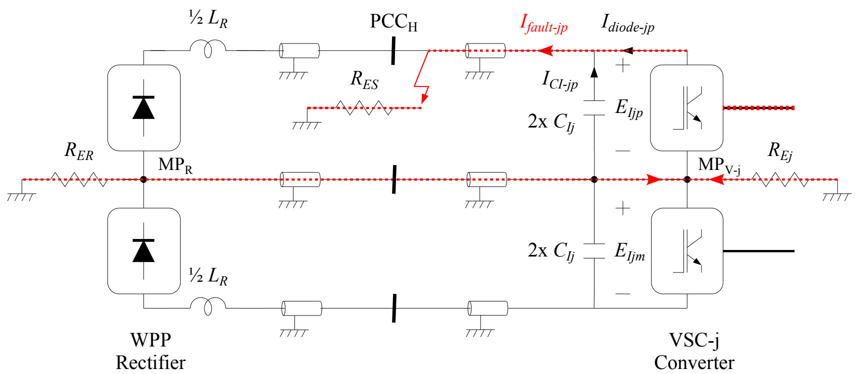

Figure 14: Pole-to-sheath short-circuit and fault current path.

4.4. *Pole-to-ground short-circuit analysis*

Fig. 14 shows the fault current path for a pole-to-sheath short-circuit. R_{ER}, R_{ES} and R_{Ej} are the resistances of the connections between ground and MP_R, sheath and MP_{Vj}, respectively. Note that there are four fault currents as there are four radial terminals connected to PCC_H.

If the midpoints of the VSCs were floating then fault currents would be reduced but, at the same time, the midpoint voltages to ground would increase too much. PSCAD simulation shows that in VSC1 the peak of the fault current $I_{diode,1p}$ is reduced from 10.1 pu to 3.9 pu but the peak voltage increases from 0.02 pu to 0.64 pu. Another option is to connect the midpoints of the VSCs to ground through a surge arrester. In this case the peak voltage decreases to 0.14 pu but the peak current increases to 7.5 pu. In this paper the midpoints of the terminals are connected to ground as it is shown in Fig. 14, but a fast HVDC breaker like the one tested in [9] must be added to avoid the large fault currents.

The VSC1 response to the pole-to-sheath short-circuit is shown in fig. 15. The detection of the sharp $E_{I,1p}$ voltage reduction will trip the ac-breaker with a delay of about 100 ms. This voltage does not reach 0 pu due to the ground and cable resistances. The negative pole keeps its voltage ($E_{I,1m}$) close to 1 pu because the fault current paths are the metallic returns and ground connections, fig. 14.

The energy reduction of the VSC1 capacitor is the reason for the capacitor current ($I_{CI,1p}$) peak of 6 pu. Then the freewheel diodes of VSC1 turn it into a rectifier with a short circuit at the dc side. The fault current $I_{fault,1p}$ has a large peak of 10.5 pu and a steady-state value of 4.5 pu which is limited by the VSC transformer impedance and the on-shore ac-grid impedance. During the short-circuit the ac-current of phase-A of VSC1 ($I_{VA,1p}$) shows large values and the corresponding ac-voltage is reduced to about 0.2 pu.

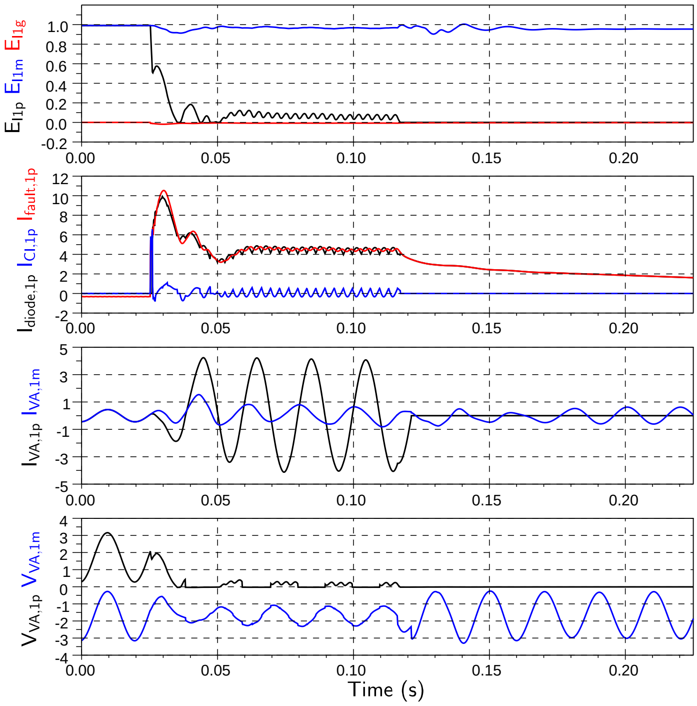

Figure 15: VSC1 response during the short-circuit at PCC_H.

5. Conclusions

This paper has introduced the connection of a large off-shore WPP to a HVdc grid by means of a diode rectifier station. The system topology and control strategies have been validated by means of PSCAD simulations.

In order to improve transient result accuracy, the HVdc cables have been simulated in detail, by using a PSCAD frequency dependent model based on the cable physical parameters.

The proposed topology and control strategy allows for the energization of the complete HVdc grid, to help service restoration in the case of an on-shore black-out.

An optimal droop-based HVdc grid control has been introduced, in order to minimize cable losses without the need of communications.

The proposed topology and control method allowed for reliable steady state and transient operation, including HVdc rectifier breaker trip and reclosure, on-shore ac-grid short circuit and HVdc link short-circuits.

During on-shore ac-grid short circuits, the complete system behaves as a single power plant and complies with current grid codes regarding fault-ride-through performance.

Moreover, the wind-turbine based VDCOL keeps the fault currents through the rectifier station and cable within reasonable limits during both HVdc and on-shore ac grid faults.

Table A.2: System Parameters

Aggregated Wind Turbines		
Front-end: 5.4 kVcc, 2 kVac, 50 Hz		
T_{Wi}: 2/33 kV	R_{Wi} = 0.005 pu	L_{Wi} = 0.06 pu
Rated powers: 5, 40, 80, 120, 155 MW		
HVdc Rectifier (based on Cigre benchmark model [28])		
Capacitor Bank: C_F = 93.53 μF		
ZF-low frequency filter		
C_{a1} = 187.1 μF	C_{a2} = 2079 μF	L_a = 4.874 mH
R_{a1} = 1.063 Ω	R_{a2} = 9.357 Ω	
ZF-high frequency filter		
C_b = 187.1 μF	R_b = 2.977 Ω	L_b = 0.4859 mH
Transformer T_{R1} and T_{R2}		
33/61/61 kV, 242 MVA	$L_{R,lk}$ = 0.18 pu	$L_{R,m}$ = 0.01 pu
dc-smoothing reactor: L_R = 200 mH		
HVdc VSCs and ac-grids		
$VSC_{j,p}$: 150 kVcc, 200 MW, 75 kVac, 50 Hz, $C_{I\,j,p}$ = 71 μF		
$T_{Vj,p}$: 75/400 kV, 250 MVA, $R_{V\,j,p}$ = 0.01 pu, $L_{V\,j,p}$ = 0.17 pu		
ac-grid: 400 kV, 500 MVA, Scc=2.0 pu, 80^o		

Table A.3: Control Parameters

VSCs PI Controller Parameters		
d-current:	K_P = 3.112	K_I = 342
q-current:	K_P = 3.112	K_I = 342
VSCs Voltage Droop Parameters		
E_{Ilow1} = 146.25 kV	k_{droop1} =	0.17778 kA/kV
E_{Ilow3} = 146.25 kV	k_{droop3} =	0.08889 kA/kV

Acknowledgements

The authors would like to thank the support of the Spanish Ministry of Economy and European Union FEDER Funds under grant DPI2014-53245-R.

Appendix A. System parameters

Tables A.2 and A.3 show the values of the system and control parameters.

References

References

[1] ABB, Technical description of HVDC Light Technology, Elanders, Vasteras, POW-0038, rev. 5 ed., 2008.

[2] M. Aragüés-Peñalba, A. Egea-Álvarez, S. Garceran Arellano, O. Gomis-Bellmunt, Droop control for loss minimization in HVDC multi-terminal transmission systems for large offshore wind farms, Electric Power Systems Research 112 (2014) 48–55. doi:10.1016/j.epsr.2014.03.013.

[3] S. Bernal-Perez, S. Añó-Villalba, R. Blasco-Gimenez, N. Aparicio, Connection of off-shore wind power plants to vsc-mtdc networks using hvdc diode-rectifiers, in: Industrial Electronics (ISIE), 2013 IEEE International Symposium on, pp. 1–6. doi:10.1109/ISIE.2013.6563795.

[4] S. Bernal-Pérez, S. Añó-Villalba, R. Blasco-Gimenez, J. Rodriguez-D'Derlée, Off-shore wind farm grid connection using a novel diode-rectifier and VSC-inverter based HVDC transmission link, in: IECON 2011 - 37th Annual Conference on IEEE Industrial Electronics Society, pp. 3186–3191. doi:10.1109/IECON.2011.6119820.

[5] R. Blasco-Gimenez, S. Añó-Villalba, J. Rodriguez-D'Derlée, S. Bernal-Pérez, F. Morant, Diode-Based HVdc link for the connection of large offshore wind farms, Energy Conversion, IEEE Transactions on 26 (2011) 615–626. doi:10.1109/TEC.2011.2114886.

[6] R. Blasco-Gimenez, S. Añó-Villalba, J. Rodríguez-D'Derlée, F. Morant, S. Bernal-Pérez, Distributed voltage and frequency control of offshore wind farms connected with a Diode-Based HVdc link, Power Electronics, IEEE Transactions on 25 (2010) 3095–3105. doi:10.1109/TPEL.2010.2086491.

[7] J. Bowles, Multiterminal HVDC transmission systems incorporating diode rectifier stations, Power Apparatus and Systems, IEEE Transactions on PAS-100 (1981) 1674–1678. doi:10.1109/TPAS.1981.316562.

[8] M.K. Bucher, M.M. Walter, M. Pfeiffer, C. Franck, Options for ground fault clearance in hvdc offshore networks, in: Energy Conversion Congress and Exposition (ECCE), 2012 IEEE, pp. 2880–2887. doi:10.1109/ECCE.2012.6342371.

[9] M. Callavik, A. Blomberg, J. Häfner, B. Jacobson, The hybrid hvdc breaker. an innovation breakthrough enabling reliable hvdc grids, ABB Grid Systems, Technical Paper Nov2012 (2012) 1–10.
[10] X. Chen, W. Lin, H. Sun, J. Wen, N. Li, L. Yao, LCC based MTDC for grid integration of large onshore wind farms in Northwest China, in: Power and Energy Society General Meeting, 2011 IEEE, pp. 1–10.
[11] CIGRE Working Groups B4-57 and B4-58, The cigre b4 dc grid test system, International Council for Large Electric Systems (2013) 1–12.
[12] L. Colla, S. Lauria, F. Palone, Short circuit and induced voltage transient study on a planned 1000 mw hvdc-vsc cable link, in: Power System Transients (IPST), 2011 International Conference on, pp. 1–6.
[13] F. Deng, Z. Chen, Design of protective inductors for hvdc transmission line within dc grid offshore wind farms, Power Delivery, IEEE Transactions on 28 (2013) 75–83. doi:10.1109/TPWRD.2012.2224384.
[14] J. Dragan, Offshore wind farm with a series multiterminal CSI HVDC, Electric Power Systems Research 78 (2008) 747–755. doi:10.1016/j.epsr.2007.05.023.
[15] EWEA, Building a stable future, The European Wind Energy Association, Annual report, 2013 (2013).
[16] S. Hungsasutra, R. Mathur, Unit connected generator with diode valve rectifier scheme, Power Systems, IEEE Transactions on 4 (1989) 538–543.
[17] M. Karystianos, Y. Kabouris, T. Koronides, S. Sofroniou, Operation of the electrical system of crete in interconnection with the mainland grid: A stability study, in: Bulk Power System Dynamics and Control - IX Optimization, Security and Control of the Emerging Power Grid (IREP), 2013 IREP Symposium, pp. 1–8. doi:10.1109/IREP.2013.6629345.
[18] P. Kundur, Power System Stability and Control, McGraw-Hill, Inc., 1994.
[19] J. Liang, T. Jing, O. Gomis-Bellmunt, J. Ekanayake, N. Jenkins, Operation and control of multiterminal HVDC transmission for offshore wind farms, Power Delivery, IEEE Transactions on 26 (2011) 2596–2604.
[20] W. Lu, B. Ooi, Optimal acquisition and aggregation of offshore wind power by multiterminal voltage-source HVDC, Power Delivery, IEEE Transactions on 18 (2003) 201–206.
[21] T. Machida, I. Ishikawa, E. Okada, E. Karasawa, Control and protection of HVDC systems with diode valve converter, Name: Electr. Eng. Jpn.(Engl. Transl) (1978).
[22] J.A. Martinez-Velasco, Power System Transients: Parameter Determination, CRC Press, 2010.
[23] A. Morched, B. Gustavsen, M. Tartibi, A universal model for accurate calculation of electromagnetic transients on overhead lines and underground cables, IEEE Transactions on Power Delivery 14 (1999) 1032–1038. doi:10.1109/61.772350.
[24] F. Mura, C. Meyer, R. De Doncker, Stability analysis of high-power dc grids, in: Industrial Commercial Power Systems Technical Conference - Conference Record 2009 IEEE, pp. 1–8. doi:10.1109/ICPS.2009.5463964.
[25] S. Muyeen, R. Takahashi, J. Tamura, Operation and control of HVDC-Connected offshore wind farm, Sustainable Energy, IEEE Transactions on 1 (2010) 30–37. doi:10.1109/TSTE.2010.2041561.
[26] W. Pan, Y. Chang, H. Chen, Hybrid multi-terminal HVDC system for large scale wind power, in: Power Systems Conference and Exposition, 2006. PSCE '06. 2006 IEEE PES, pp. 755–759.
[27] E. Prieto-Araujo, F. Bianchi, A. Junyent-Ferré, O. Gomis-Bellmunt, Methodology for droop control dynamic analysis of multiterminal vsc-hvdc grids for offshore wind farms, Power Delivery, IEEE Transactions on 26 (2011) 2476–2485.
[28] M. Szechtman, T. Wess, C.V. Thio, First benchmark model for HVDC control studies, Electra 135 (1991) 54–73.
[29] L. Wang, K.H. Wang, Dynamic stability analysis of a dfig-based offshore wind farm connected to a power grid through an hvdc link, Power Systems, IEEE Transactions on 26 (2011) 1501–1510. doi:10.1109/TPWRS.2010.2085053.
[30] J. Yang, J. Fletcher, J. O'Reilly, Short-circuit and ground fault analyses and location in vsc-based dc network cables, Industrial Electronics, IEEE Transactions on 59 (2012) 3827–3837. doi:10.1109/TIE.2011.2162712.
[31] L. jie Zhao, H. Rao, X. lin Li, W. Zhang, Y. Xiang, M. li Fu, Development of ±160 kv xlpe cable and its application to the world's first three-terminal vsc hvdc system in china, in: CIGRÉ AORC Technical Meeting, B1-1110, pp. 1–7.